Inorganic Chemistry
ARTICLE
pubs.acs.org/IC

Synthesis, Crystal Structures, Photophysical Properties, and Bioimaging of Living Cells of Bis-β-Diketonate Phenothiazine Ligands and Its Cyclic Dinuclear Complexes

Dongmei Li,[†] Xiaohe Tian,[‡] Guiju Hu,[†] Qiong Zhang,[†] Peng Wang,[†] Pingping Sun,[†] Hongping Zhou,[†] Xiangming Meng,[†] Jiaxiang Yang,[†] Jieying Wu,[†] Baokang Jin,[†] Shengyi Zhang,[†] Xutang Tao,[§] and Yupeng Tian[*,†,§,⊥]

[†]Department of Chemistry, Key Laboratory of Functional Inorganic Materials of Chemistry of Anhui Province, Anhui University, Hefei 230039, P.R. China

[‡]Department of Biomedical Science, University of Sheffield, Sheffield, U.K.

[§]State Key Laboratory of Crystal Materials, Shandong University, Jinan 250100, P.R. China

[⊥]State Key Laboratory of Coordination Chemistry, Nanjing University, Nanjing 210093, P.R. China

S *Supporting Information*

ABSTRACT: Two bis-β-diketones, $RCOCH_2CO$-EPTZ-$COCH_2COR$ (EPTZ = 10-ethylphenothiazine; R = C_6H_5 for H_2L^1 and CF_3 for H_2L^2) and their cyclic dinuclear Zn(II), Cd(II), Ni(II), Mn(II), Cu(II), Co(II) complexes have been synthesized and fully characterized. Their crystal structures were determined by single crystal X-ray diffraction analysis. Their photophysical properties have been further investigated both experimentally and theoretically. The results revealed that significant enhancement of two-photon absorption cross section values were obtained for the cyclic dinuclear Zn(II) and Cd(II) complexes compared with their free ligands. Additionally, confocal microscopy and two-photon microscopy fluorescent imaging of MCF-7 cells labeled with two ligands and Zn(II) complexes reveal their potential applications as a biological fluorescent probe.

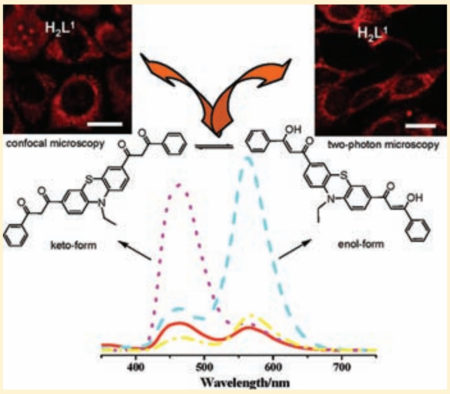

INTRODUCTION

Two-photon absorption (TPA) has significant advantages over conventional one-photon absorption, which has led to applications in microfabrication,[1] optical data storage,[2] photodynamic therapy,[3] up-converted lasing,[4] and microscopy.[5] Two-photon microscopy (TPM) becomes one of the most important tools in fluorescence microscopy of thick tissues and in live animal cells. This technique offers many advantages over conventional confocal microscopy, including increased penetration depth, localized excitation, and prolonged observation time.[6] Therefore, considerable research efforts have been devoted to the development of new chromophores with large two-photon absorption (TPA) cross sections (δ) for the use in biological imaging, such as polymers,[7] small organic molecules,[8] semiconductor or metal nanoparticles,[9] and coordination compounds.[10] There are already numerous reports on multiphoton bioimaging using coordination metal Zn[11] and lanthanide complexes[12] as multiphoton luminescent bioimaging. Lam et al.[13] reported the use of organometallic platinum(II) complexes for a potential multiphoton luminescent probe for in vitro bioimaging. Also, a series of selected cyclometalated platinum(II) complexes have also been fully explored by Botchway et al.,[14] as two-photon emission live cell imaging. However, the coordination compounds with large two-photon absorption cross sections have been scarcely systemically studied, as well as the application in two-photon biological imaging.

In this Article, first, 10-ethylphenothiazine (EPTZ) was selected as the D (donor) group, because electron-rich phenothiazines (PTZs) possess two important aspects that make it an ideal building block for photoluminescence (PL) and electroluminescence (EL) molecular materials: (i) PTZ is a strong electron donor due to its low oxidation potential ($E_{1/2}$ = +0.59 V in acetonitrile vs SCE);[15] (ii) unlike N-substituted carbazoles, the nonplanar PTZ ring structure restricts π-stacking aggregation, which may lead generally to a detrimental quenching of the luminescence in the solid state.[16] Second, β-diketonate derivatives can act as good bidentate ligands, after losing a proton, coordinating to metal ions to form π-conjugated unit. Therefore, bis-β-diketone ligands can form a higher degree of π-electron delocalization in the cyclic

Received: January 22, 2011
Published: August 09, 2011

dinuclear metal complexes due to an extended π-bridge by π-electron contribution from the metal ions. Significantly, their dinuclear metal complexes should possess excellent photophysical, electrochemical, biological, and magnetic properties.[17]

On the basis of our interest in searching for optimized molecular structures having large molecular TPA cross sections, two novel ligands were constructed by combining phenothiazine with two β-diketone units. In order to perform detailed investigations on the structure and photophysical properties, diverse complexes have been synthesized by using a series of transition metals [nickel(II), manganese(II), copper(II), cobalt(II)], and closed-shell d^{10}-metals [zinc(II), cadmium(II)], among them, the closed-shell d^{10} metal complexes which would more likely lead to enhanced TPA properties due to the lack of d−d transitions in comparison with the others. First, the photophysical properties of the bis-β-diketones as ligand were pre-explored both experimentally and theoretically before the preparations of the metal complexes. And then, the properties of all the complexes were systematically investigated. Finally, the potential applications in biological imaging using confocal microscopy and two-photon scanning microscopy of MCF-7 cells labeled with two ligands and their dinuclear Zn(II) complexes were captured, respectively.

EXPERIMENTAL SECTION

Materials and Apparatus. All solvents were dried and purified by usual methods. Elemental analysis was performed with a Perkin-Elmer 240 analyzer. IR spectra (4000−400 cm^{-1}), as KBr pellets, were recorded on a Nicolet FT-IR 170 SX spectrophotometer. The mass spectra were obtained on a Micromass GCT-MS spectrometer and a Bruker reflex TOF mass spectrometer (Bruker-Franzen Analytik, Bremen, Germany). ^{1}H and ^{13}C NMR spectra were performed on a Bruker 400 spectrometer with tetramethylsilane (Si(CH$_3$)$_4$) as the internal standard. Thermogravimetric analysis (TGA) was recorded with a Perkin-Elmer Pris-1 DMDA-V1 analyzer in an atmosphere of nitrogen at a heating rate of 10 °C min^{-1}.

3,7-Di(3-phenyl-3-oxopropanoyl)-10-ethylphenothia-zine H_2L^1. Potassium *t*-butanolate (1.12 g, 10 mmol), 20 mL of methyl benzoate, and **A**[18] (1 g, 3.2 mmol) were added into a 50 mL flask. The mixture was stirred at room temperature for 8 h and poured into 400 mL of brine. Addition of dilute H$_2$SO$_4$ to the orange solution yielded the red oil. After the removal of the water, the products were precipitated by the addition of petroleum ether (500 mL). Red solids were collected by filtration. The product was purified by chromatography on a silica gel with ethyl acetate/petroleum ether mixture (v/v 1/2) as the eluent. Red microcrystals were obtained, yield: 1.0 g (60%). GC/MS: (m/z) 519.04 (M$^+$), 490.03 (M$^+$ − C$_2$H$_5$). ^{1}H NMR (400 MHz, CDCl$_3$) δ (ppm): 1.51 (t, J = 7.2 and 7.2 Hz, 3H), 4.04 (q, J = 6.3, 6.3, and 6.3 Hz, 2H), 6.78 (s, 2H), 6.95 (d, J = 8.4 Hz, 2H), 7.51 (t, J = 7.8 and 7.2 Hz, 4H), 7.58 (t, J = 7.2 and 7.2 Hz, 2H), 7.73 (s, 2H), 7.83 (d, J = 8.4 Hz, 2H), 7.99 (d, J = 7.2 Hz, 4H), 16.9 (s, 2H). ^{13}C NMR (100 MHz, d_6-CD$_3$COCD$_3$) δ (ppm): 12.00, 42.37, 54.06, 92.41, 115.38, 122.87, 126.00, 127.14, 127.76, 128.72, 130.23, 132.49, 135.18, 147.33, 153.56, 197.54. IR (KBr) (cm^{-1}): 2977 and 2918 (ν_{C-H}, aliphatic), 1605 ($\nu_{C=O}$, carbonyl), 1575, 1551, and 1456 ($\nu_{C=C}$, aromatic), 768 (γ_{C-H}, aromatic). Anal. Calcd for C$_{32}$H$_{25}$NO$_4$S: C, 73.97; H, 4.85; N, 2.70; O, 12.32; S, 6.17%. Found: C, 73.73; H, 4.90; N, 2.88; O, 12.17; S, 6.32%. Red, block crystals of **H$_2$L^1** suitable for single crystal X-ray diffraction analysis were obtained by slow evaporation of CH$_2$Cl$_2$/petroleum ether mixture (v/v 4/1).

3,7-Di(3-trifluoromethyl-3-oxopropanoyl)-10-ethyl-phenothiazine H_2L^2. In a 100 mL flask, 60 mL of ethanol and sodium (2.3 g, 0.1 mol) were added. After the sodium was completely exhausted, **A** (1 g, 3.2 mmol) was added. The mixture was cooled over the ice−water bath. After 1 h, 10 mL of ethyl trifluoroacetate was added in one portion. The mixture was stirred for another 8 h, and then poured into ice water. Addition of dilute H$_2$SO$_4$ to the orange solution yielded the red solid, which was collected by filtration and recrystallized from acetone to give the desired product, yield: 0.97 g (65%). GC/MS: (m/z) 503.06 (M$^+$), 474.03 (M$^+$ − C$_2$H$_5$). ^{1}H NMR (400 MHz, d_6-DMSO) δ (ppm): 1.35 (t, J = 8.5 and 8.5 Hz, 3H), 4.02 (q, J = 8.2, 8.7, and 8.5 Hz, 2H), 6.29 (s, 2H), 7.07 (d, J = 11 Hz,2H), 7.79 (s, 2H), 7.84 (d, J = 8.5 Hz, 2H), 16.6 (s, 2H). ^{13}C NMR (100 MHz, d_6-DMSO) δ (ppm): 12.64, 42.83, 89.19, 115.43, 122.06, 126.44, 128.22, 133.14, 148.57, 150.40, 185.88, 201.57. IR (KBr) (cm^{-1}): 2990 and 2925 (ν_{C-H}, aliphatic), 1623 ($\nu_{C=O}$, carbonyl), 1577, 1551, and 1476 ($\nu_{C=C}$, aromatic), 1305 and 1130 (ν_{C-F}, trifluoromethyl), 786 (γ_{C-H}, aromatic). Anal. Calcd for C$_{22}$H$_{15}$F$_6$NO$_4$S: C, 52.49; H, 3.00; N, 2.78; O, 12.71; S, 6.37%. Found: C, 52.56; H, 3.04; N, 2.90; O, 12.61; S, 6.28%.

Synthesis of the Complexes. M(OAc)$_2\cdot n$H$_2$O (0.13 mmol) and bis-β-diketones (0.06 mmol) were dissolved in 5 mL of pyridine. The solution was stirred at room temperature until a lot of precipitation formed and was then filtered. The crude product was washed by dichloromethane (15 mL × 3) and then CH$_3$CN (15 mL × 3). (Details of the complexes **2**−**6** and **8**−**12** are shown in Supporting Information.)

$[Zn_2Py_4L^1{}_2]\cdot 2Py$ (1). Orange, block crystals of **1** suitable for single crystal X-ray diffraction analysis were obtained by slow evaporation of the remaining pyridine solution. Yield: 23 mg (47%). ^{1}H NMR (400 MHz, d_6-DMSO) δ (ppm): 1.41 (t, J = 7.0 and 7.0 Hz, 6H), 4.08 (q, J = 6.8, 7.0, and 6.8 Hz, 4H), 6.81 (s, 4H), 7.07 (d, J = 8.5 Hz, 4H), 7.39 (m, 12H), 7.51 (m, 12H), 7.79 (t, J = 7.8 and 7.5 Hz, 6H), 7.93 (s, 4H), 8.04 (d, J = 8.8 Hz, 4H), 8.10 (d, J = 7.0 Hz, 8H), 8.58 (s, 12H). ^{13}C NMR (100 MHz, d_6-DMSO) δ (ppm): 12.72, 42.38, 91.62, 115.04, 121.96, 124.41, 126.52, 127.60, 128.80, 131.67, 134.52, 136.69, 140.79, 145.90, 150.04, 183.53, 185.71. IR (KBr) (cm^{-1}): 2977 and 2918 (ν_{C-H}, aliphatic), 1589 ($\nu_{C=O}$, carbonyl), 758 and 700 (γ_{C-H}, pyridine). Anal. Calcd for C$_{94}$H$_{76}$N$_8$O$_8$S$_2$Zn$_2$: C, 68.82; H, 4.67; N, 6.83; O, 7.80; S, 3.91%. Found: C, 68.76; H, 4.51; N, 6.91; O, 7.77; S, 3.82%. TGA analysis: the first weight loss occurred at 100 °C corresponding to the loss of two solvent pyridine rings (9.6%). The second weight loss occurred at 250 °C corresponding to the loss of four coordinated pyridine units (19.2%). The main structure decomposed at 435 °C.

$[Zn_2Py_2L^2{}_2]\cdot 2THF$ (7). The crude product from the synthesis of complex **7** was again dissolved in THF, and orange plate crystals suitable for single crystal X-ray diffraction analysis were obtained in a few days, yield: 30 mg (73%). ^{1}H NMR (400 MHz, d_6-DMSO) δ (ppm): 1.37 (t, 6H), 1.76 (m, 8H), 3.1 (m, 8H), 4.05 (q, 4H), 6.75 (s, 4H), 6.95 (d, 4H), 7.39 (m, 4H), 7.53 (m, 2H), 7.79 (t, 4H), 7.95 (s, 4H), 8.75 (d, 4H). IR (KBr) (cm^{-1}): 2985 and 2923 (ν_{C-H}, aliphatic), 1620 ($\nu_{C=O}$, carbonyl), 1136 (ν_{C-F}, trifluoromethyl), 755 and 698 (γ_{C-H}, pyridine). Anal. Calcd for C$_{62}$H$_{52}$F$_{12}$N$_4$O$_{10}$S$_2$Zn$_2$: C, 51.86; H, 3.65; N, 3.90; O, 11.14; S, 4.47%. Found: C, 51.78; H, 3.69; N, 4.07; O, 11.25; S, 4.61%. TGA analysis: the first weight loss occurred at 130 °C corresponding to the loss of two THF molecules (9.0%). The second weight loss occurred at 200 °C corresponding to the loss of four coordinated pyridine units (19.8%). The main structure decomposed at 390 °C.

Optical Measurements. The linear absorption spectra were measured on a UV−3600 spectrophotometer. The one-photon excited fluorescence (OPEF) spectra measurements were performed using an F-2500 fluorescence spectrophotometer. The concentration of sample solution is 10 μM. The dianion species (**L**)$^{2-}$ were obtained by adding 2 equiv of NaOH into the THF solution of the neutral ligands.

TPA cross sections (δ) of the samples were obtained by two-photon excited fluorescence (TPEF) method at femtosecond laser pulse and Ti: sapphire system (700−900 nm, 76 MHz, 200 fs) as the light source. The concentration of sample solution is at 1.0 × 10^{-4} M. Thus, δ of samples is determined by the following equation

$$\delta_s = \delta_r \frac{F_s \cdot \Phi_r \cdot C_r \cdot n_r}{F_r \cdot \Phi_s \cdot C_s \cdot n_s}$$

where the subscripts "s" and "r" represent sample and reference (here fluorescein in ethanol solution at concentration of 1.2×10^{-4} M was used as reference), respectively. F is the overall fluorescence collection efficiency intensity of the fluorescence signal collected by the fiber spectra meter. Φ, n, and c are quantum yield of the fluorescence, refractive index of solvent, and the concentration of solution, respectively.

Cell Culture. MCF-7 cells (MCF-7 human breast cancer cell line) were seeded in six-well plates at a density of 2×10^5 cells per well and grown for 96 h.[19] For live-cell imaging, cell cultures were incubated with complex solution and maintained at 37 °C under 5% CO_2/95% air for 2 h of incubation time. The cells were then washed with PBS (3 × 3 mL per well), and PBS (3 mL) was added to each well.

Cell Image. Cells were seeded in 6 well plates at a density of 2×10^5 cells per well and grown for 96 h. For live cell imaging cell cultures were incubated with the complexes (10% PBS/90% cell media) at concentrations 50 μM and maintained at 37 °C in an atmosphere of 5% CO_2 and 95% air for incubation times ranging for 2 h. The cells were then washed with PBS (3 × 3 mL per well), and 3 mL of PBS was added to each well. The cells were imaged using confocal laser scanning microscopy and water immersion lenses. Excitation energy of 720 nm was used, and the fluorescence emission was measured at 650–700 nm.

Microscopy. MCF-7 cells were luminescently imaged on a Zeiss LSM 510 META upright confocal laser scanning microscope using magnification 40× and 100× water-dipping lenses for monolayer cultures. Image data acquisition and processing was performed using Zeiss LSM Image Browser, Zeiss LSM Image Expert and Image J.

Cytotoxicity Assays in Cells. To ascertain the cytotoxic effect of all the compounds treatment over a 24-h period, the 5-dimethylthiazol-2-yl-2,5-diphenyltetrazolium bromide (MTT) assay was performed. HeLa cells were passed and plated to ~70% confluence in 96-well plates 24 h before treatment. Prior to the compounds' treatment, the DMEM was removed and replaced with fresh DMEM, and aliquots of the compound stock solutions (500 μM DMSO) were added to obtain final concentrations of 10, 20, 50, and 100 μM. The treated cells were incubated for 24 h at 37 °C and under 5% CO_2. Subsequently, the cells were treated with 5 mg/mL MTT (40 μL/well) and incubated for an additional 4 h (37 °C, 5% CO_2). Then, DMEM was removed, the cells were dissolved in DMSO (150 μL/well), and the absorbance at 570 nm was recorded. The cell viability (%) was calculated according to the following equation: cell viability % = $OD_{570(\mathrm{sample})}/OD_{570(\mathrm{control})} \times 100$, where $OD_{570(\mathrm{sample})}$ represents the optical density of the wells treated with various concentration of the compounds and $OD_{570(\mathrm{control})}$ represents that of the wells treated with DMEM + 10% FCS. Three independent trials were conducted, and the averages and standard deviations are reported. The reported percent cell survival values are relative to untreated control cells.

Computational Studies. The optimization was done by B3LYP (6-31G(d))[20] with C_s symmetry constraints. Then, TDDFT (B3LYP (6-31G(d,p)) calculations[21] were performed on the optimized structure. All the calculations including optimizations and TDDFT were conducted in G03 software.[22] Geometry optimization of the singlet ground state and TDDFT calculation of the lowest 20 singlet–singlet excitation energies were calculated with a basis set composed by 6-31G* for C, H, N, O atoms,[23] and the 6-31G* basis set for S was downloaded from the EMSL basis set library.[24] An analytical frequency analysis provides evidence that the calculated species represents a true minimum without imaginary frequencies on the respective potential energy surface. In the calculation of the optical absorption spectrum, the 20 lowest spin-allowed singlet–singlet transitions, up to energy of ~5 eV, were taken into account.

X-ray Crystallography. Single crystal X-ray diffraction measurements were carried out on a Siemens Smart 1000 CCD diffractmeter equipped with a graphite crystal monochromator situated in the incident beam for data collection at room temperature. The determination of unit cell parameters and data collections were performed with Mo Kα radiation (λ = 0.71073 Å). Unit cell dimensions were obtained with least-squares refinements, and all structures were solved by direct methods with SHELXL–97.[25] All the non-hydrogen atoms were located in successive difference Fourier syntheses. The final refinement was performed by full-matrix least-squares methods with anisotropic thermal parameters for non-hydrogen atoms on F^2. The hydrogen atoms were added theoretically and riding on the concerned atoms. Cambridge Crystallographic Data Centre (CCDC) information as supplementary publication numbers follow: CCDC $\mathbf{H_2L^1}$–298940, **1**–660612, **7**–673738, **8**–711281, **9** –660613, **10**–673759, **11**–700927, **12**–700930.

RESULTS AND DISCUSSION

Through the Claisen condensation reaction, 3,7-diacetyl-10-ethylphenothiazine reacted with methyl benzoate and ethyl trifluoroacetate to give $\mathbf{H_2L^1}$ and $\mathbf{H_2L^2}$ in high yields, respectively (Scheme 1). The ^{1}H NMR spectrum of $\mathbf{H_2L^2}$ shows that its enol isomer is the most dominant form even in the polar solvent d_6-DMSO. $\mathbf{H_2L^1}$ exists in the enol tautomer in $CDCl_3$ with the characteristic enolic proton signal at about δ 16.9, when it was in d_6-acetone, the percent of the β-diketone in enol decreased from 82.45% to 44.22% within one week.[17d] All the complexes were obtained in high yield by mixing bis-β-diketones with 2 equiv of $M(OAc)_2 \cdot nH_2O$ in pyridine.

Crystal Structure Determinations. The unit cell, data collection, and refinement parameters are located in Table S1 and S2. Selected bond lengths and angles are given in Tables S3–S6 (see Supporting Information).

Structure of the Ligand $\mathbf{H_2L^1}$. $\mathbf{H_2L^1}$ crystallizes in the monoclinic space group $P2_1/c$. Figure 1 shows an ORTEP plot of the molecule with the atomic numbering scheme. The result shows that the molecule of $\mathbf{H_2L^1}$ looks like a butterfly with two slightly distorted wings. The conformation of the phenothiazine molecule is folded about the S–N axis with a dihedral angle of 152.8° (Figure 1, inset). The two wings are slightly distorted; on one side, the dihedral angle between the terminal (P4) and central phenyl rings (P3) is 28.42°, and the other (between P1 and P2) is 17.59°. The linkage bond lengths between the terminal and central phenyl rings is quite conjugated with bond lengths of C(19)–C(22) [1.498(4) Å], C(22)–C(23) [1.410(5) Å], C(23)–C(24) [1.379(5) Å], and C24–C25 [1.476(4) Å] (Table S3). These structural features suggest that a highly π-conjugated system is formed by all the non-hydrogen atoms, leading to a charge transfer from donor to acceptor over the π-bridge. The bond lengths of the carbonyl units reveal that the both enolic protons are shared asymmetrically between the two carbonyl oxygen atoms, and $\mathbf{H_2L^1}$ exists in the enol form in solid state.

Structures of the Complexes. All the complexes form a dinuclear 24-membered macrocyclic ring, in which a much higher degree of π-electron delocalization shall be obtained due to the complexation.[26] Two $\mathbf{L}^{2-}$ ligands as a sandwich coordinate to two metal ions with the β-diketonate sites. Pyridine molecules bind the metal ion, affording a 5- or 6-coordination geometry about the metal center. The structures of the

Scheme 1. Synthesis of Two Bis-β-diketones H_2L^1, H_2L^2 and Their Complexes

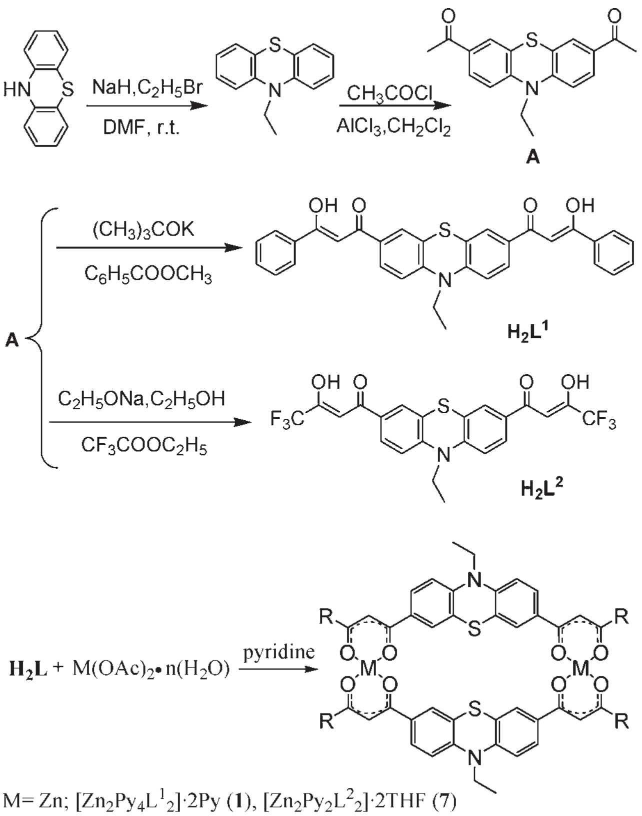

M= Zn; $[Zn_2Py_4L^1_2]{\cdot}2Py$ (**1**), $[Zn_2Py_2L^2_2]{\cdot}2THF$ (**7**)
Cd; $Cd_2Py_4L^1_2$ (**2**), $Cd_2Py_4L^2_2$ (**8**)
Ni; $[Ni_2Py_4L^1_2]{\cdot}3C_6H_6$ (**3**), $Ni_2Py_4L^2_2$ (**9**)
Mn; $Mn_2Py_4L^1_2$ (**4**), $Mn_2Py_4L^2_2$ (**10**)
Cu; $[Cu_2L^1_2]{\cdot}2DMF$ (**5**), $[Cu_2Py_2L^2_2]{\cdot}2C_6H_6$ (**11**)
Co; $Co_2Py_4L^1_2$ (**6**), $Co_2Py_4L^2_2$ (**12**)

R = 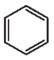 (**H_2L^1**)

R = CF_3 (**H_2L^2**)

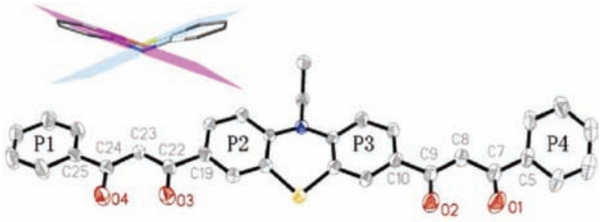

Figure 1. ORTEP structure of **H_2L^1** (with 50% thermal ellipsoid probability). Top left (inset): showing the conformation of the phenothiazine molecule folded about the S−N axis with a dihedral angle of 152.8°. All hydrogen atoms are omitted for clarity.

complexes are classified into three types (I, II, and III) with respect to the geometry about the central metal ions. All the complexes belonging to types II and III crystallize in the triclinic space group $P\bar{1}$.

Type I: Four Coordination. The structure of this type appears only in $[Cu_2L^1_2]{\cdot}2DMF$ (**5**). Compound **5** crystallizes in the monoclinic space group $P2_1/c$. Each Cu(II) center has a square planar coordinated sphere surrounded by four oxygen atoms from two β-diketonato fragments. This kind of structure has been described by us before.[26]

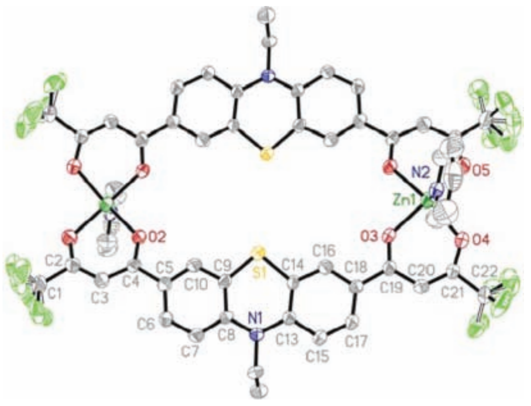

Figure 2. ORTEP structure of complex **7** with atomic labeling scheme (with 50% thermal ellipsoid probability). All hydrogen atoms and solvent molecules are omitted for clarity; there is conformational disorder of the CF_3 groups.

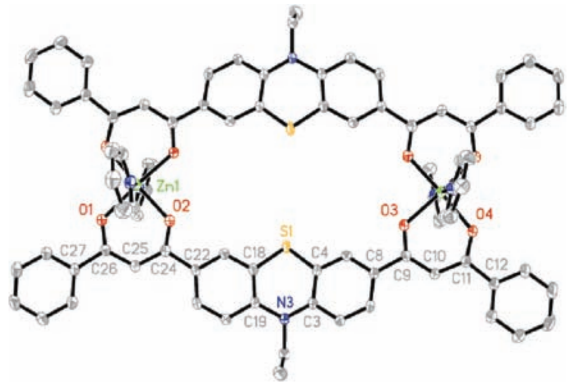

Figure 3. ORTEP structure of complex $[Zn_2Py_4L^1_2]{\cdot}2Py$ (**1**) with atomic labeling scheme (with 50% thermal ellipsoid probability); all hydrogen atoms and solvent molecules are omitted for clarity.

Type II: Five Coordination. The structures of $[Zn_2Py_2L^2_2]{\cdot}2THF$ (**7**) and $[Cu_2Py_2L^2_2]{\cdot}2C_6H_6$ (**11**) belong to this type. The ORTEP plot of **7** is shown in Figure 2 as an example. The geometry about Zn(II) is square-pyramidal with four O atoms of the two 1,3-diketonate sites on the equatorial plane and one nitrogen atom from pyridine at the apical position; the distance between the metal center and the equatorial plane is 0.400 Å. The dihedral angle between planes S1−C9−C8−N1 and S1−C14−C13−N1 is 163.12°. The S···S and Zn···Zn separations are 4.340 and 12.887 Å, respectively. Zn−O bond lengths are 1.989(5)−2.004(5) Å, and Zn1−N2 bond length is 2.028(6) Å, falling in the rational Zn−O and Zn−N bond lengths, respectively (Table S4).[27] The bond lengths are intermediate, such as O3−C19 [1.247(7) Å], O4−C21 [1.242(7) Å], C19−C20 [1.405(9) Å], and C20−C21 [1.320(9) Å], showing that there is a higher degree of electron delocalization in the dinuclear metal complexes.

Type III: Six Coordination. Each metal center in the complexes of this type ($[Zn_2Py_4L^1_2]{\cdot}2Py$ (**1**), $[Ni_2Py_4L^1_2]{\cdot}3C_6H_6$ (**3**), $[Cd_2Py_4L^2_2]$ (**8**), $[Ni_2Py_4L^2_2]$ (**9**), $[Mn_2Py_4L^2_2]$ (**10**), and $[Co_2Py_4L^2_2]$ (**12**)) adopts a pseudo-octahedral geometry with pyridine rings occupying both axial positions and oxygen donors from two β-diketone fragments binding in the equatorial positions. The ORTEP plot of **1** is shown in Figure 3 as an example

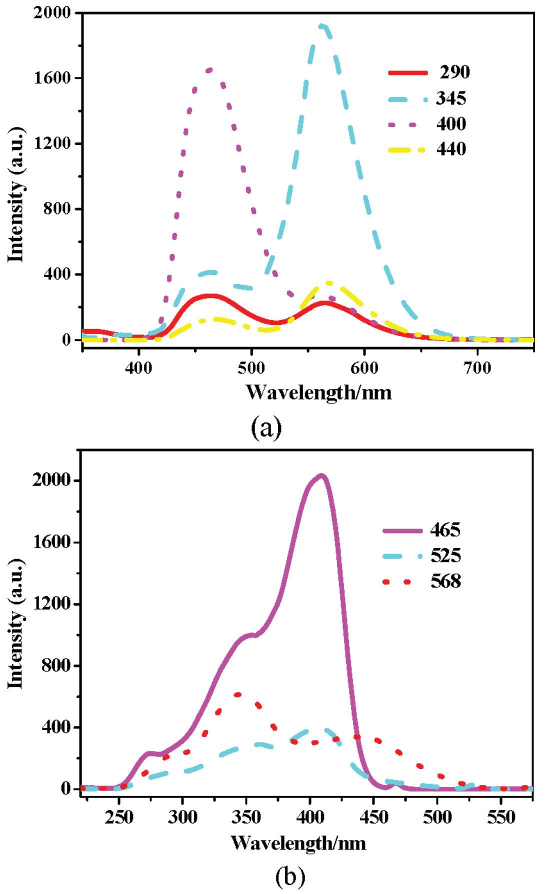

Figure 4. (a) Dependence of the steady-state fluorescence spectra of H_2L^1 on excitation wavelength. Inset: excitation wavelengths (λ_{ex}). (b) Fluorescence excitation spectra recorded for H_2L^1 for various observation wavelengths, λ_{obs} (inset). In THF, c = 10 μM.

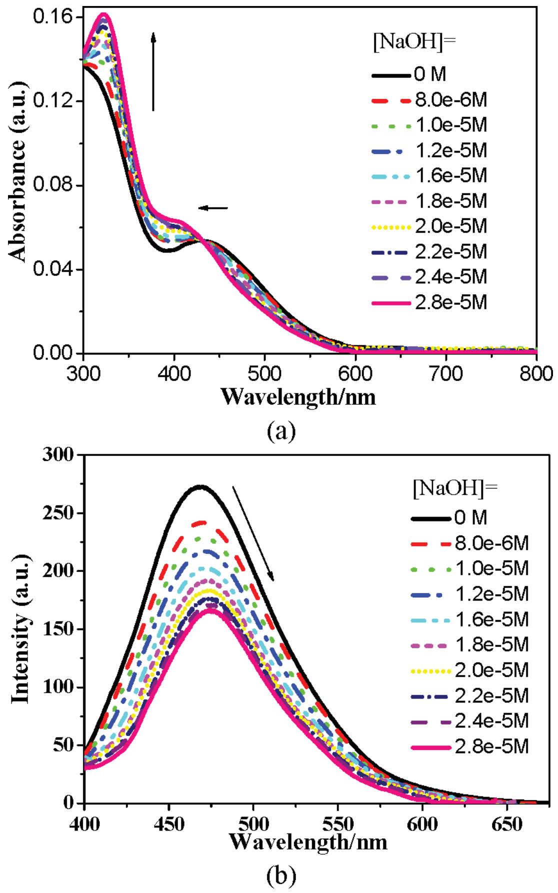

Figure 5. (a) Linear absorption and (b) OPEF spectra of H_2L^2 ([H_2L^2] = 10 μM) obtained in different NaOH concentrations.

(the molecular structures of the other complexes are shown in the Supporting Information).

Complex **1** shows little distortion with the deviation of 0.0287 Å from the equatorial coordination plane formed by one zinc atom and four oxygen donors. Two equatorial coordination spheres in the complex are coplanar. Each bis-β-diketonate ligand is slightly twisted away from the mean plane, presumably reducing steric interference. Two coordinating pyridine rings form a dihedral angle of 28.89° with each other, while the dihedral angles they formed with the equatorial coordination plane are 98.50° and 89.02°, respectively. The dihedral angle between planes S1−C4−C3−N3 and S1−C18−C19−N3 is 153.8°. The S···S and Zn···Zn separations are 5.236 and 12.753 Å, respectively. The dihedral angle between the terminal (P1) and central phenyl rings (P2) is 5.33°, and the other (between P3 and P4) is 21.40°. The bond lengths of the coordination rings are also intermediate, such as O3−C9 [1.271(4) Å], O4−C11 [1.274(4) Å], C9−C10 [1.400(5) Å], and C10−C11 [1.404(5) Å] (Table S5). A 24-membered ring structure can lead to a higher degree of delocalization in the dinuclear metal complexes. For the equatorial coordination sphere containing one Zn atom and four O atoms in the molecule of **1**, which is more coplanar than that in **7**, it may facilitate the π-electron delocalization in the complex, thus causing an enhanced TPA response in **1**.

Linear Absorption and One-Photon Excited Fluorescence (OPEF). Table S7 (see the Supporting Information) summarizes the linear absorption and fluorescence spectra for all the compounds in different solvents.

In six kinds of solvents, the absorption spectra of H_2L^1 and H_2L^2 feature an intense absorption band at 316−350 nm and a moderately intense absorption in the 414−492 nm range with extinction coefficients (ε's) on the order of 10^4 dm^3 mol^{-1} cm^{-1} (Figure S8 and S9). The one-photon fluorescence spectra of H_2L^2 in all the solvents exhibit one intense emission band at 536−582 nm. It is reconfirmed that H_2L^2 exists in its enol form in all the solvents. The peak positions and luminescence intensities are not relative to the polarity of the solvents. The OPEF spectra of H_2L^1 exhibit one emission band in the 529−572 nm range in hexane, benzene, $CHCl_3$, and DMF, but exhibit dual emission in THF and acetonitrile (Figure S8). The ratio of the intensities of the dual emission bands varies from different excitation wavelengths (Figure 4a), which is resulting from a heterogeneous sample with more than one absorbing and emitting species.[28] In this study, the keto and enol isomers of H_2L^1 emit at 462 and 567 nm, respectively. By recording fluorescence excitation spectra with different observation wavelengths (Figure 4b), it is concluded that the keto isomer mainly absorbs at 408 nm in THF, while the absorption spectra of the enol isomer exhibit three absorption bands with the strongest one at ca. 340 nm. These assignments are further corroborated by the calculation methods. The concentration-dependent studies in the range 1×10^{-6} to 1×10^{-5} M show that H_2L^1 is much more prone to exist in the keto form under lower concentration (compare Figure S8 with Figure S10). Furthermore, only one

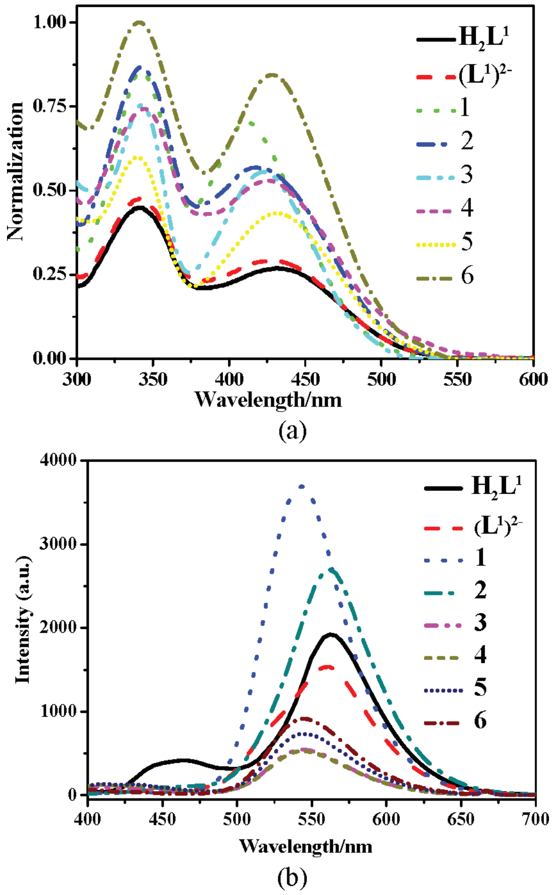

Figure 6. (a) Linear absorption and (b) OPEF spectra of $\mathbf{H_2L^1}$ and its complexes in THF.

solid-state emission observed for $\mathbf{H_2L^1}$ at 621 nm is in agreement with the X-ray diffraction analysis that $\mathbf{H_2L^1}$ exists in its enol form in the solid state (Table S7). Obviously, different keto−enol tautomeric equilibria exist for the ligands with two different terminal groups, R = phenyl (π-electron group) $\mathbf{H_2L^1}$ and R = CF_3 (strong electron-withdrawing group) $\mathbf{H_2L^2}$.

In Figure 5, the (a) linear absorption and (b) OPEF spectra of $\mathbf{H_2L^2}$ ([$\mathbf{H_2L^2}$] = 10 μM) in water are given in different NaOH concentrations. With increasing [NaOH], the enol moieties are deprotonated, and three different species are expected: undeprotonated, monodeprotonated, and doubly deprotonated. From Figure 5a, it can be seen that doubly deprotonated species $(\mathbf{L^2})^{2-}$ is expected to be present in the concentration of [NaOH] = 2×10^{-5} M; the high-energy absorption shows a red-shifted λ_{ab} value, while the low-energy absorption is much blue-shifted. According to the calculations, the low-energy absorption of $\mathbf{H_2L^2}$ (λ = 462 nm and f = 0.37) is assigned as the intramolecular charge transfer (ICT) transition [$\pi_{PTZ} \rightarrow \pi^*_{COCHC(OH)CF3}$] due to the H → L transition (vide infra). However, for $(\mathbf{L^2})^{2-}$, the outer enol moieties become the electron rich fragments, and we expect a net charge transfer to the internal PTZ fragment.[29] It is reconfirmed by the computational data that the low-energy absorption band (λ = 389.10 nm and f = 0.18) is caused by HOMO → LUMO transition and assigned as [π $(CF_3COCHCO)^- \rightarrow \pi^*$ (PTZ)] (Figure S11). The OPEF spectra (Figure 5b) show red-shifted λ_{em} value accompanying with decreasing in intensity.

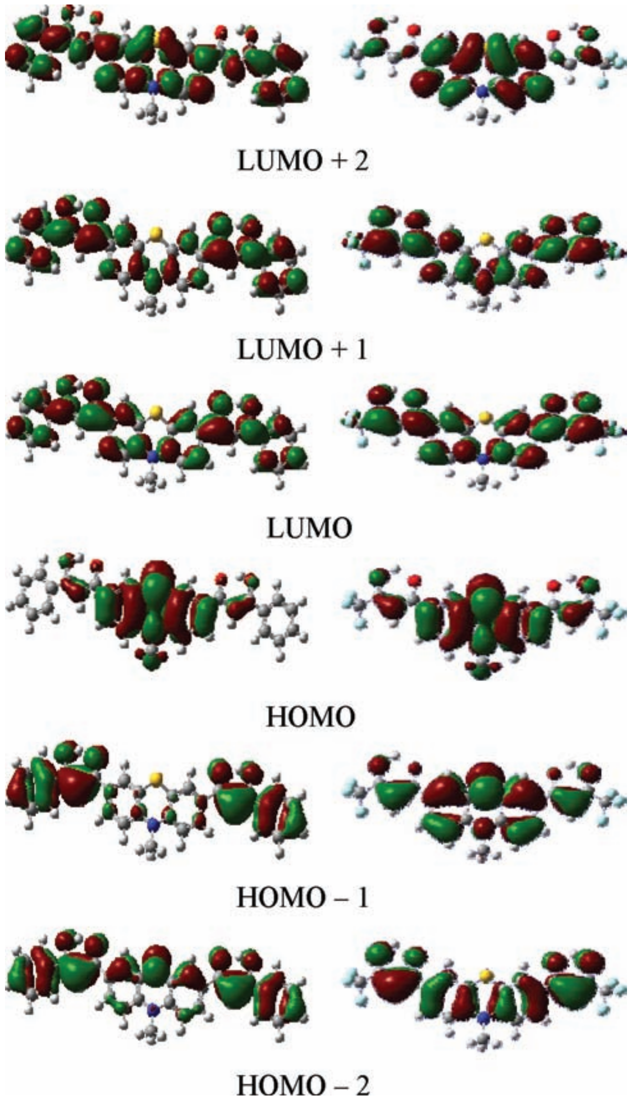

Figure 7. Spatial plots of the selected frontier molecular orbitals of the enol form of $\mathbf{H_2L^{1'}}$ (left) and $\mathbf{H_2L^{2'}}$ (right). The time-dependent hybrid density functional theory (TDDFT) calculations were performed using B3LYP/6-31G*//6-31G**.

The same shift tendency in the absorption maxima of the complexes in THF was observed for that of $(\mathbf{L})^{2-}$ compared to their neutral counterparts (Figures 6and S12 and Table S7). The OPEF spectra of the complexes **7**−**12** and $(\mathbf{L^2})^{2-}$ show a red-shifted λ_{em} value compared to that of $\mathbf{H_2L^2}$. Considering each complex molecule containing the two ligand groups, the increases in fluorescence intensities were only observed for complexes **7** and **8** relative to those of $(\mathbf{L^2})^{2-}$ and $\mathbf{H_2L^2}$. The OPEF spectrum of $\mathbf{H_2L^1}$ shows that the keto emission was absent upon deprotonation, because the bis-β-diketone loses protons only through its enol form (Figure 6). The one-photon fluorescence spectra of complexes **1**−**6** and $(\mathbf{L^1})^{2-}$ show blue-shifted λ_{em} values compared to the enol emission of $\mathbf{H_2L^1}$. Only the OPEF intensities of **1** and **2** largely increased compared to that of the real ligand $(\mathbf{L^1})^{2-}$. It may be inferred that the high conjugation in the 24-membered ring system, and the closed-shell d^{10}-metal centers (Zn and Cd), are both responsible for the increased fluorescence intensity.

Table 1. Selected Low-Lying Singlet (S_n) Excited States Computed by TDDFT Method with the Orbitals Involved (OI) in the Excitations Including Transition Coefficients (Tc), Excitation Energies (eV and nm), and Oscillator Strengths (f) in $H_2L^{1'}$ and $H_2L^{2'}$

S_n	character	OI	Tc[a]	E_{ex}[b]	f[c]
		$H_2^{L^{1'}}$			
S_1	ICT	H → L	0.68	2.78/446.4	0.50
S_3	$\pi \rightarrow \pi^*(COCHC(OH)C_6H_5$[d]	H − 2 → L	0.52	3.69/335.9	0.71
S_6	$\pi_{PTZ} \rightarrow \pi^*_L$[e]	H → L + 2	0.62	3.80/326.3	0.37
		$H_2^{L^{2'}}$			
S_1	ICT	H → L	0.67	2.68/462.0	0.37
S_3	$\pi_{C(OH)CHCO(PTZ)COCHC(OH)} \rightarrow \pi^*_{COCHC(OH)CF3}$	H − 1 → L	0.61	3.66/338.5	0.36
S_7	$\pi \rightarrow \pi^*(PTZ)$[f]	H → L + 2	0.63	3.99/310.7	0.56
S_9	$\pi_{C(OH)CHCO(PTZ)COCHC(OH)} \rightarrow \pi^*_{PTZ}$	H − 2 → L + 2	0.65	4.17/297.4	0.41

[a] The excitations with the transition coefficients less than 0.4 were not shown. [b] Excitation energy in eV/nm. [c] Only the singlet excited stated with $f > 0.3$ were listed. [d] $\pi \rightarrow \pi^*$ transition delocalized over the $COCHC(OH)C_6H_5$ system. [e] π orbital on PTZ unit → π^* orbital on the whole molecule. [f] $\pi \rightarrow \pi^*$ transition of PTZ.

Computational Studies. TDDFT computational studies have been performed to elucidate the electronic structures of the ground state of the two ligands. Here, model compounds, $\mathbf{H_2L^{1'}}$ and $\mathbf{H_2L^{2'}}$, were used instead of $\mathbf{H_2L^1}$ and $\mathbf{H_2L^2}$, in which the ethyl group on the PTZ was replaced by methyl group (for details, see the Experimental Section). The spatial plots of selected TDDFT frontier molecular orbitals were shown in Figure 7. The energies of the frontier orbitals and the percentage compositions of these frontier orbitals were listed in Table 1.

The HOMOs (H) of $\mathbf{H_2L^{2'}}$ and $\mathbf{H_2L^{1'}}$ are of π orbitals localized on the PTZ. The unoccupied molecular orbitals LUMO (L) and L + 1 are the COCHC(OH)R units. The L + 2 of $\mathbf{H_2L^{2'}}$ is a π^* orbital on PTZ. The H − 1 and H − 2 of $\mathbf{H_2L^{2'}}$ are π orbitals on C(OH)CHCO(PTZ)COCHC(OH). L + 2 of $\mathbf{H_2L^{1'}}$ is a π^* orbital localized on the whole molecule (denoted as π^*_L). The H − 1 and H − 2 of $\mathbf{H_2L^{1'}}$ are π orbitals on COCHC(OH)C_6H_5.

As shown in Table 1, the lowest-energy excitation bands of the two ligands ($\lambda = 446$ nm and $f = 0.50$ for $\mathbf{H_2L^{1'}}$, $\lambda = 462$ nm and $f = 0.37$ for $\mathbf{H_2L^{2'}}$) are assigned as the ICT transition [$\pi_{PTZ} \rightarrow \pi^*_{COCHC(OH)R}$] due to the H → L transition. The HOMO−LUMO energy gap of $\mathbf{H_2L^{2'}}$ (2.68 eV) is much smaller than that of $\mathbf{H_2L^{1'}}$ (2.78 eV), caused by the different terminal units in the two ligands. It is obvious that the strong electron-withdrawing CF_3 unit used instead of the π-electron C_6H_5 moiety can cause an increase of ICT in $\mathbf{H_2L^{2'}}$. Several transitions are computed in the high- energy absorption regions of both ligands. The band of $\mathbf{H_2L^{1'}}$ is mainly due to the H − 2 → L transition [$\pi \rightarrow \pi^*(COCHC(OH)C_6H_5)$], whereas that of $\mathbf{H_2L^{2'}}$ is probably due to the H − 1 → L transition [$\pi_{C(OH)CHCO(PTZ)COCHC(OH)} \rightarrow \pi^*_{COCHC(OH)CF3}$] mixed with the H → L + 2 transition [$\pi \rightarrow \pi^*$(PTZ)]. It is inferred that the oscillator strengths of the high-energy absorption bands of both ligands are larger than those of the low-energy bands. Basically, the calculated singlet−singlet transitions in $\mathbf{H_2L^{2'}}$ and $\mathbf{H_2L^{1'}}$ are in reasonable agreement with the experimental λ_{ab} in the two major absorption bands observed.

TDDFT computational studies have been also performed to the keto form of $\mathbf{H_2L^1}$. It is found that the main excitation band ($\lambda = 402$ nm, $f = 0.22$) is assigned as [$\pi \rightarrow \pi^*$ (CO(PTZ)CO)] due to the H → L transition (Figure 8). It is agreed with the experimental result that the main absorption band was found at 408 nm upon excitation at 465 nm in THF (Figure 4b).

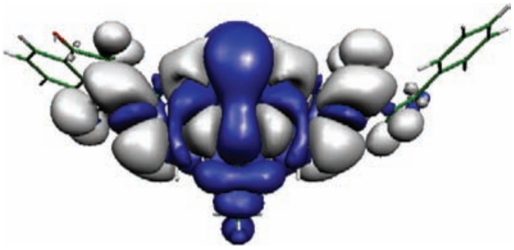

Figure 8. Density difference between the charge-transfer and ground states of the keto form of $\mathbf{H_2L^1}$ in the gas phase. The blue and gray part represents the electron loss and gain, respectively.

Two-Photon Excited Fluorescence (TPEF). As shown in Figures 6 and S12, there is no linear absorption in the wavelength range 550−900 nm for all the compounds in THF, which indicates that there are no energy levels corresponding to an electron transition in this spectral range. If frequency upconverted fluorescence appears upon excitation with a tunable laser in this range, it should be safely attributed to multiphoton absorption excited fluorescence. (The detailed information is in Supporting Information.)

Detailed experiments revealed that the peak positions of the TPEF spectra of these chromophores are independent of the excitation wavelengths, but the emission intensities of the TPEF are dependent on the excitation wavelengths. The electrons can be pumped to the different excited states by TPA due to the different selection rules, but they would finally relax to the same lowest excited state via internal conversion and/or vibrational relaxation.[2] By tuning the pump wavelengths incrementally from 700 to 900 nm, keeping the input power fixed, the TPEF intensities were recorded. Upon excitation at the optimal wavelengths, the TPEF spectra of the compounds in THF are presented in Figure 9. No TPEF signals of complexes **3**−**6** and **9**−**12** were detected. The TPEF peaks of **1**, **2**, and $(\mathbf{L^1})^{2-}$ are blue-shifted compared to that of $\mathbf{H_2L^1}$. While the TPEF peaks of **7**, **8**, and $(\mathbf{L^2})^{2-}$ are red-shifted compared to that of $\mathbf{H_2L^2}$. Upon deprotonation, the TPEF intensities of $(\mathbf{L^1})^{2-}$ and $(\mathbf{L^2})^{2-}$ are both decreased largely relative to those of their respective neutral counterparts. As a consequence, the TPEF intensities of complexes **1**, **2** and **7**, **8** are much increased compared to those of their real ligands $(\mathbf{L^1})^{2-}$ and $(\mathbf{L^2})^{2-}$, respectively.

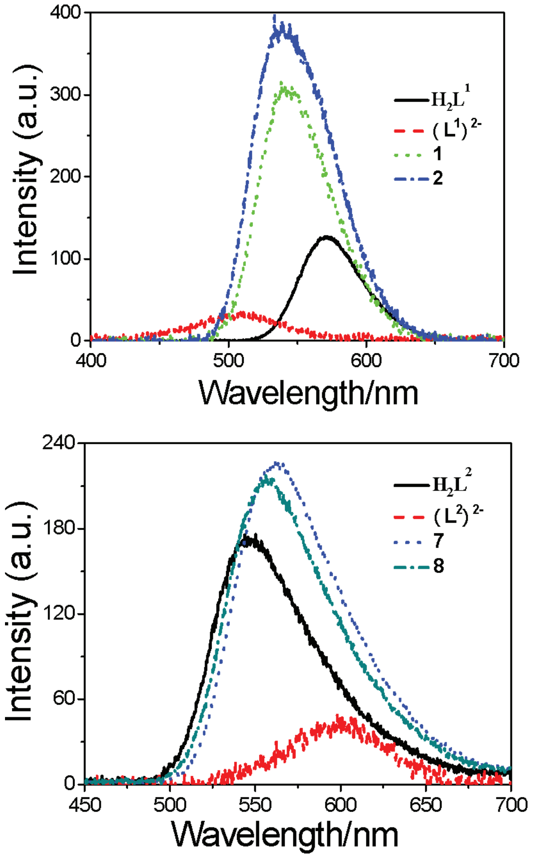

Figure 9. TPEF spectra of all compounds in THF with $c = 0.1$ mM at the optimal excitation wavelength.

The TPA spectra of the compounds in THF are presented in Figure 10. It is shown that the peak δ values for $\mathbf{H_2L^1}$ and $\mathbf{H_2L^2}$ are ca. 155 (700 nm) and 204 GM (710 nm), respectively. The electron-accepting ability of the groups is $CF_3 > C_6H_6$, which corresponds to the order in δ. The enhancement of δ was explained in terms of increased charge separation assisted by the terminal strong electron-withdrawing groups. Upon deprotonation, δ_{max} values of $(\mathbf{L^1})^{2-}$ and $(\mathbf{L^2})^{2-}$ are largely decreased compared to those of $\mathbf{H_2L^1}$ and $\mathbf{H_2L^2}$, respectively. Considering each complex molecule containing two ligand molecules, δ_{max} values of **1** and **2** are ca. 568 and 664 GM at 710 nm, 14- and 16-fold larger than that of the real ligand $(\mathbf{L^1})^{2-}$. And the peak δ values for **7** and **8** are ca. 369 (710 nm) and 366 GM (720 nm), 7-fold larger than that of the real ligand $(\mathbf{L^2})^{2-}$. Thus, the dramatically increased fluorescence can be achieved by using the closed-shell d^{10}-metal centers such as Zn^{2+} and Cd^{2+}. An extended π-bridge considering the π-electron contribution from the metal ions, in the 24-membered ring system of the complex, may favor the ICT, thus causing an enhanced two-photon absorption.[30] An enhanced TPA response found in **1** rather than **7** may be caused by the equatorial coordination sphere being more coplanar in **1** than in **7**, leading to a higher degree of π-electron delocalization, which is proved by the crystal structures.

Live Cell Images of Confocal Microscopy and Two-Photon Microscopy. As Zn has relatively low toxicity toward live cells, fluorescent images of confocal microscopy and two-photon microscopy of MCF-7 cells labeled with two ligands and their dinuclear Zn(II) complexes ($\mathbf{H_2L^1}$, $\mathbf{H_2L^2}$, **1**, and **7**) were captured, respectively. All compounds were first dissolved in

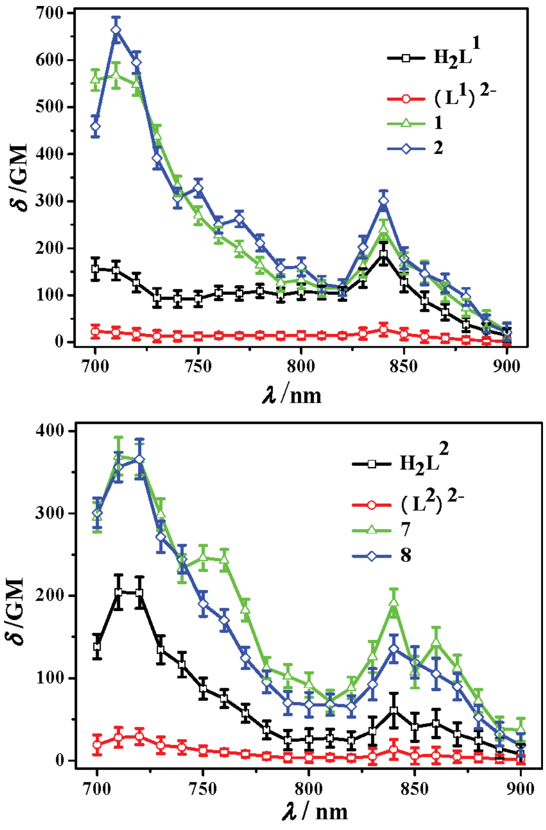

Figure 10. TPA spectra of all the compounds ($c = 0.1$ mM) in THF.

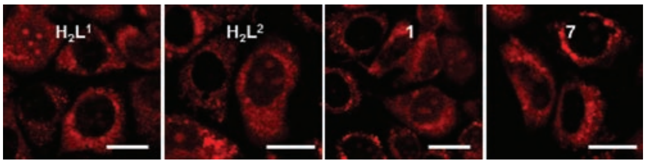

Figure 11. Fluorescent imaging of confocal microscopy of MCF-7 cells at one-photon image, $\lambda_{ex} = 458$ nm, from left to right: $\mathbf{H_2L^1}$, $\mathbf{H_2L^2}$, **1**, and **7** (all the scale bars represent 10 μm).

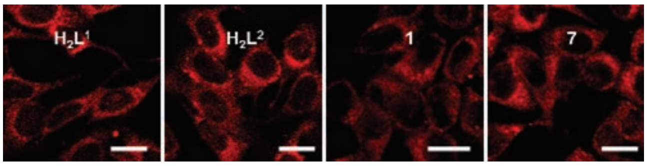

Figure 12. Fluorescent imaging of two-photon microscopy of MCF-7 cells, $\lambda_{ex} = 720$ nm, from left to right: $\mathbf{H_2L^1}$, $\mathbf{H_2L^2}$, **1**, and **7** (all the scale bars represent 10 μm).

DMSO to 20 mM, then diluted by PBS (phosphate buffer solution) to 50 μM. MCF-7 cells (human breast cancer cell line) incubated with 50 μM of $\mathbf{H_2L^1}$, $\mathbf{H_2L^2}$, **1**, and **7**, respectively, in growth media at 37 °C, 5% CO_2 for 2 h, then washed by PBS and directly moved to confocal laser scanning microscopy without fixation. The fluorescent images of confocal microscopy and two-photon microscopy show that the chromophores are presented within the cells (Figures 11 and 12). Similar fluorescent images of confocal microscopy ($\lambda_{ex} = 458$ nm) were obtained from $\mathbf{H_2L^1}$,

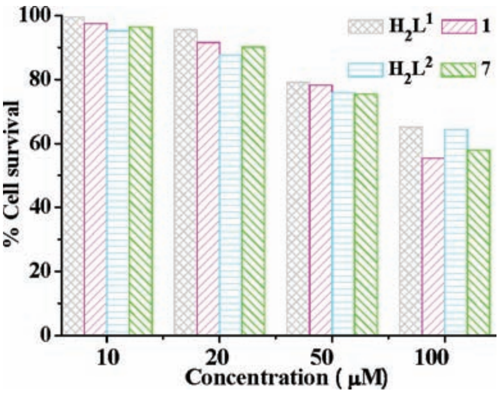

Figure 13. Cytotoxicity data results obtained from the MTT assay.

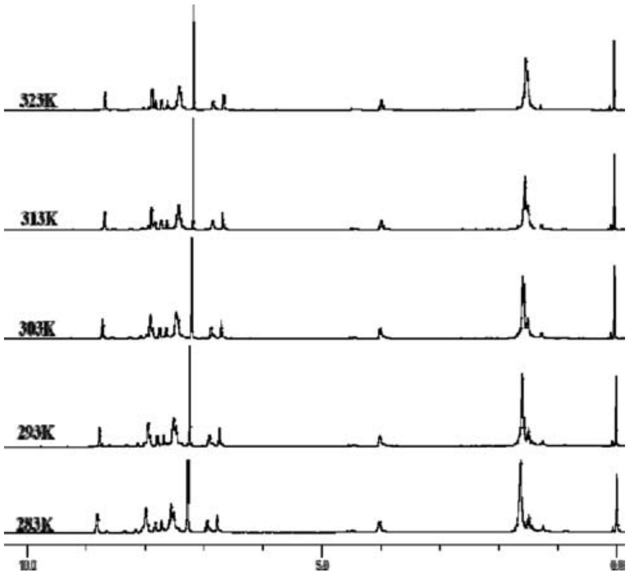

Figure 14. Variable temperature ^{1}H NMR of $\mathbf{Zn_2Py_2L^2{}_2}$.

$\mathbf{H_2L^2}$, **1**, and **7**, respectively. Herein, the cytoplasmic distribution is more uniform. A few bright spots are observed in the nucleus indicating that the compounds may target small organelles in the nuclear region called nucleoli.[31] The fluorescent images of two-photon microscopy of all the four compounds exhibit similar cellular cytosol uptake at the excitation wavelength of 720 nm compared with one photon excitation. It is showing the remarkable stability of the fluorescence which from cellular cytosol as we switch one photon excitation to two photon excitation, as known the disadvantage of photon-damage for current fluorescent agent, this series complexes might be able to have potential as more safety fluorescence probe. Cytotoxicity is a potential side effect that must be controlled when dealing with living cells or tissues. So cytotoxicity assays were investigated in HeLa cells by the MTT assay (Figure 13, more information is shown in Supporting Information, Table S8). These cytotoxicity tests show that sub- and low-micromolar concentrations of the compounds are essentially nontoxic over a period of at least 24 h and could safely be used for further biological studies. To further prove the stability of the complex, the variable temperature ^{1}H NMR of $\mathbf{Zn_2Py_2L^2{}_2}$ has been measured (Figures 14 and S14). MALDI-TOF mass spectrometry was used to further verify the stability of complex **7** in water solution, which was first dissolved in a small amount of DMSO, and then diluted with water. The result suggests the complex is very stable in water solution, which belongs to the molecular weight of the structure $\mathbf{Zn_2L^2{}_2}$ (more detailed information is shown in Figure S15).

■ CONCLUSIONS

Two bis-β-diketones, $\mathbf{H_2L^1}$, $\mathbf{H_2L^2}$, and their cyclic dinuclear Zn(II), Cd(II), Ni(II), Mn(II), Cu(II), and Co(II) complexes have been synthesized and fully characterized. The results show that the two different terminal groups of the bis-β-diketone ligands can cause different tautomeric equilibrium both experimentally and theoretically. The keto and enol forms of $\mathbf{H_2L^1}$ with phenyl group coexist in several solvents, such as THF and acetonitrile. $\mathbf{H_2L^2}$ with CF_3, a strong electron-withdrawing group, only shows the photophysical properties of its enol form in all the solvents. Besides, an increased δ for $\mathbf{H_2L^2}$ was explained in terms of increased charge separation assisted by the terminal strong electron-withdrawing groups. More intensive OPEF and TPEF, and much increased δ values, were obtained for the cyclic dinuclear Zn(II) and Cd(II) complexes compared to those of their free ligands. It is inferred that the much increased fluorescence can be achieved by using the closed-shell d^{10}-metal centers, such as Zn^{2+} and Cd^{2+}. An extended π-bridge considering the π-electron contribution from the metal ions, in the 24-membered ring system of the complex, may favor the ICT, thus causing an enhanced two-photon absorption. The fluorescent images of both confocal microscopy and two-photon microscopy of MCF-7 cells labeled with two ligands and their Zn(II) complexes show strong emissions. However, the highly conjugated dinuclear Zn(II) complexes are better candidates for the TPM images because of their larger δ and low toxicity to the lively cells. This work paves the way for the designation of either the novel types of bis-β-diketones or their complexes or new effective chromophores with two-photon active for TPM images of live cells.

■ ASSOCIATED CONTENT

Ⓢ **Supporting Information.** X-ray crystallographic data for $\mathbf{H_2L^1}$ and complexes **1** and **7**−**12** in CIF format. Linear absorption and OPEF spectra of $\mathbf{H_2L^1}$ and $\mathbf{H_2L^2}$, spatial plots of the selected frontier molecular orbitals of the enol form of $(\mathbf{L^2})^{2-}$, and crystallographic data. This material is available free of charge via the Internet at http://pubs.acs.org.

■ AUTHOR INFORMATION

Corresponding Author

*E-mail: yptian@ahu.edu.cn.

■ ACKNOWLEDGMENT

This work was supported by a grant from the National Natural Science Foundation of China (21071001, 50873001), Education Committee of Anhui Province (KJ2009A52, KJ2010A030), the Team for Scientific Innovation Foundation of Anhui Province (2006KJ007TD), Science and Technological Fund of Anhui Province for Outstanding Youth (10040606Y22), and the 211 Project of Anhui University, Ministry of Education Funded Projects, focus on returned overseas scholar.

■ REFERENCES

(1) (a) He, G. S.; Tan, L. S.; Zheng, Q.; Prasad, P. N. *Chem. Rev.* **2008**, *108*, 1245–1330. (b) Tian, Y. P.; Li, L.; Zhang, J. Z.; Yang, J. X.; Zhou, H. P.; Wu, J. Y.; Sun, P.; Tao, L.; Guo, Y.; Wang, C.; Xing, H.; Huang, W.; Tao, X.; Jiang, M. *J. Mater. Chem.* **2007**, *17*, 3646–3654.

(2) Li, L.; Tian, Y. P.; Yang, J. X.; Sun, P. P.; Wu, J. Y.; Zhou, H. P.; Zhang, S. Y.; Jin, B. K.; Xing, X. J.; Wang, C. K.; Li, M.; Cheng, G. H.; Tang, H. H.; Huang, W. H.; Tao, X. T.; Jiang, M. H. *Chem—Asian J.* **2009**, *4*, 668–680.

(3) (a) Celli, J. P.; Spring, B. Q.; Rizvi, I.; Evans, C. L.; Samkoe, K. S.; Verma, S.; Pogue, B. W.; Hasan, T. *Chem. Rev.* **2010**, *110*, 2795–2838. (b) Kim, S.; Ohulchanskyy, T. Y.; Pudavar, H. E.; Pandey, R. K.; Prasad, P. N. *J. Am. Chem. Soc.* **2007**, *129*, 2669–2675.

(4) Pawlicki, M.; Collins, H. A.; Denning, R. G.; Anderson, H. L. *Angew. Chem., Int. Ed.* **2009**, *48*, 3244–3266.

(5) (a) Kim, H. M.; Cho, B. R. *Chem. Commun.* **2009**, 153–164. (b) Au, L.; Zhang, Q.; Cobley, C. M.; Gidding, M.; Schwartz, A. G.; Chen, J.; Xia, Y. *ACS Nano* **2010**, *4*, 35–42. (c) Chalal, M.; Ehrburger-Dolle, F.; Morfin, I.; Vial, J.; Armas, M. A.; Roman, J. S.; Bölgen, N.; Piçkin, E.; Ziane, O.; Casalegno, R. *Macromolecules* **2009**, *42*, 2749–2755.

(6) (a) Williams, R. M.; Zipfel, W. R.; Webb, W. W. *Curr. Opin. Chem. Biol.* **2001**, *5*, 603–608. (b) Zipfel, W. R.; Williams, R. M.; Webb, W. W. *Nat. Biotechnol.* **2003**, *21*, 1369–1377. (c) Wang, B. G.; König, K.; Halbhuber, K. J. *J. Microsc.* **2010**, *238*, 1–20.

(7) Hayek, A.; Ercelen, S.; Zhang, X.; Bolze, F.; Nicoud, J. F.; Schaub, E.; Baldeck, P. L.; Mély, Y. *Bioconjugate Chem.* **2007**, *18*, 844–851.

(8) (a) Kim, H. M.; Seo, M. S.; An, M. J.; Hong, J. H.; Tian, Y. S.; Choi, J. H.; Kwon, O.; Lee, K. J.; Cho, B. R. *Angew. Chem., Int. Ed.* **2008**, *47*, 5167–5170. (b) Kim, M. K.; Lim, C. S.; Hong, J. T.; Han, J. H.; Jang, H. Y.; Kim, H. M.; Cho, B. R. *Angew. Chem., Int. Ed.* **2010**, *49*, 364–367. (c) Lee, J. H.; Lim, C. S.; Tian, Y. S.; Han, J. H.; Cho, B. R. *J. Am. Chem. Soc.* **2010**, *132*, 1216–1217. (d) Shao, J. J.; Guan, Z. P.; Yan, Y. L.; Jiao, C. J.; Xu, Q. H; Chi, C. *J. Org. Chem.* **2011**, *76*, 780–790. (e) Mausumi, C.; Mehboob Alam, M. M.; Chakrabarti, S. *J. Phys. Chem. A* **2011**, *115*, 2607–2614.

(9) (a) Stewart, M. E.; Anderton, C. R.; Thompson, L. B.; Maria, J.; Gray, S. K.; Rogers, J. A.; Nuzzo, R. G. *Chem. Rev.* **2008**, *108*, 494–521. (b) Cao, L.; Wang, X.; Meziani, M. J.; Lu, F. S.; Wang, H. F.; Luo, P. G.; Lin, Y.; Harruff, B. A.; Veca, L. M.; Murray, D.; Xie, S. Y.; Sun, Y. P. *J. Am. Chem. Soc.* **2007**, *129*, 11318–11319. (c) Yong, K. T.; Ding, H.; Roy, I.; Law, W. C.; Bergey, E. J.; Maitra, A.; Prasad, P. N. *ACS Nano* **2009**, *3*, 502–510. (d) Padilha, L. A.; Nootz, G.; Olszak, P. D.; Webster, S.; Hagan, D. J.; Stryland, E. W. V.; Levina, L.; Sukhovatkin, V.; Brzozowski, L.; Sargent, E. H. *Nano Lett.* **2011**, *11*, 1227–1231. (e) Zhu, M. Q.; Zhang, G. F.; Li, C.; Aldred, M. P.; Chang, E.; Drezek, R. A.; Li, A. D. Q. *J. Am. Chem. Soc.* **2011**, *133*, 365–372.

(10) (a) Haas, K. L.; Franz, K. J. *Chem. Rev.* **2009**, *109*, 4921–4960. (b) Picot, A.; D'Aléo, A.; Baldeck, P. L.; Grichine, A.; Duperray, A.; Andraud, C.; Maury, O. *J. Am. Chem. Soc.* **2008**, *130*, 1532–1533. (c) Gao, Y. H.; Wu, J. Y.; Li, Y. M.; Sun, P. P.; Zhou, H. P.; Yang, J. Y.; Zhang, S. Y.; Jin, B. K.; Tian, Y. P. *J. Am. Chem. Soc.* **2009**, *131*, 5208–5213. (d) Sumalekshmy, S.; Fahrni, C. J. *Chem. Mater.* **2011**, *23*, 483–500.

(11) (a) Chang, C. J.; Nolan, E. M.; Jaworski, J.; Okamoto, K. I.; Hayashi, Y.; Sheng, M.; Lippard, S. J. *Inorg. Chem.* **2004**, *43*, 6774–6779. (b) Taki, M.; Wolford, J. L.; O'Halloran, T. V. *J. Am. Chem. Soc.* **2004**, *126*, 712–713. (c) Huang, C.; Qu, J.; Qi, J.; Yan, M.; Xu, G. X. *Org. Lett.* **2011**, *13*, 1462–1465.

(12) (a) Andraud, C.; Maury, O. *Eur. J. Inorg. Chem.* **2009**, 4357–4371. (b) Duan, C. K.; Tanner, P. A. *J. Phys. Chem. A* **2011**, *115*, 1922–1932.

(13) Koo, C. K.; Wong, K. L.; Man, C. W. Y.; Lam, Y. W.; So, L. K.-Y.; Tam, H. L.; Tsao, S. W.; Cheah, K. W.; Lau, K. C.; Yang, Y. Y.; Chen, J. C.; Lam, M. H.-W. *Inorg. Chem.* **2009**, *48*, 872–878.

(14) Botchway, S. W.; Charnley, M.; Haycock, J. W.; Parker, A. W.; Rochester, D. L.; Weinstein, J. A.; Williams, J. A. G. *Proc. Natl. Acad. Sci. U.S.A.* **2008**, *105*, 16071–16076.

(15) (a) Nath, S.; Pal, H.; Palit, D. K.; Sapre, A. V.; Mittal, J. P. *J. Phys. Chem. A* **1998**, *102*, 5822−5830. (b) Nocera, D. G.; Gray, H. B. *J. Am. Chem. Soc.* **1981**, *103*, 7349−7350.

(16) (a) Panozzo, S.; Vial, J. C.; Kervella, Y.; Stéphan, O. *J. Appl. Phys.* **2002**, *92*, 3495−3502. (b) Kim, G. W.; Cho, M. J.; Yu, Y. J.; Cho, D. H. *Chem. Mater.* **2007**, *19*, 42–50.

(17) (a) Grillo, V. A.; Seddon, E. J.; Grant, C. M.; Aromí, G.; Bollinger, J. C.; Folting, K.; Christou, G. *Chem. Commun.* **1997**, 1561−1562. (b) Shiga, T.; Ohba, M.; Ohkawa, H. *Inorg. Chem.* **2004**, *43*, 4435−4436. (c) Clegg, J. K.; Lindoy, L. F.; Moubaraki, B.; Murray, K. S.; McMurtrie, J. C. *Dalton Trans.* **2004**, 2417−2423. (d) Schweitzer, G. K.; Benson, E. W. *J. Chem. Eng. Data* **1968**, *13*, 452−453.

(18) Li, D. M.; Zhou, H. P.; Pu, J. Q.; Feng, X. J.; Wu, J. Y.; Tian, Y. P.; Yu, X. Q.; Tao, X. T.; Jiang, M. H. *Chin. J. Chem.* **2005**, *23*, 1483.

(19) Tian, X.; Gill, M. R.; Cantón, I.; Thomas, J. A.; Battaglia, G. *ChemBioChem* **2011**, *12*, 548–551.

(20) Yang, L.; Feng, J. K.; Ren, A. M. *J. Org. Chem.* **2005**, *70*, 5987–5996.

(21) Li, D. M.; Hu, R. T.; Zhou, W.; Sun, P. P.; Kan, Y.; Tian, Y. P.; Zhou, H. P.; Wu, J. Y.; Tao, X. T.; Jiang, M. H. *Eur. J. Inorg. Chem.* **2009**, *2009*, 2664–2672.

(22) Frisch, M. J.; Trucks, G. W.; Schlegel, H. B.; Scuseria, G. E.; Robb, M. A.; Cheeseman, J. R.; Montgomery, J. A., Jr.; Vreven, T.; Kudin, K. N.; Burant, J. C.; Millam, J. M.; Iyengar, S. S.; Tomasi, J.; Barone, V.; Mennucci, B.; Cossi, M.; Scalmani, G.; Rega, N.; Petersson, G. A.; Nakatsuji, H.; Hada, M.; Ehara, M.; Toyota, K.; Fukuda, R.; Hasegawa, J.; Ishida, M.; Nakajima, T.; Honda, Y.; Kitao, O.; Nakai, H.; Klene, M.; Li, X.; Knox, J. E.; Hratchian, H. P.; Cross, J. B.; Adamo, C.; Jaramillo, J.; Gomperts, R.; Stratmann, R. E.; Yazyev, O.; Austin, A. J.; Cammi, R.; Pomelli, C.; Ochterski, J. W.; Ayala, P. Y.; Morokuma, K.; Voth, G. A.; Salvador, P.; Dannenberg, J. J.; Zakrzewski, V. G.; Dapprich, S.; Daniels, A. D.; Strain, M. C.; Farkas, O.; Malick, D. K.; Rabuck, A. D.; Raghavachari, K.; Foresman, J. B.; Ortiz, J. V.; Cui, Q.; Baboul, A. G.; Clifford, S.; Cioslowski, J.; Stefanov, B. B.; Liu, G.; Liashenko, A.; Piskorz, P.; Komaromi, I.; Martin, R. L.; Fox, D. J.; Keith, T.; Al-Laham, M. A.; Peng, C. Y.; Nanayakkara, A.; Challacombe, M.; Gill, P. M. W.; Johnson, B.; Chen, W.; Wong, M. W.; Gonzalez, C.; Pople, J. A. *Gaussian 03, Revision B.04*; Gaussian, Inc.: Pittsburgh, PA, 2003.

(23) Angelis, F. D.; Fantacci, S.; Sgamellotti, A.; Cariati, E.; Ugo, R.; Ford, P. C. *Inorg. Chem.* **2006**, *45*, 10576–10584.

(24) EMSL basis set library available at http://www.emsl.pnl.gov/forms/basisform.html.

(25) Sheldrick, G. M. *SHELXL-97: Program for Crystal Structure Refinement*; University of Göttingen: Göttingen, Germany, 1997.

(26) Li, D. M.; Zhou, W.; Xu, G. Y.; Zhou, H. P.; Wu, J. Y.; Tian, Y. P.; Tao, X. T.; Jiang, M. H. *J. Mol. Struct.* **2009**, *929*, 120–124.

(27) Gushchin, P. V.; Luzyanin, K. V.; Kopylovich, M. N.; Haukka, M.; Pombeiro, A. J. L.; Kukushkin, V. Y. *Inorg. Chem.* **2008**, *47*, 3088–3094.

(28) Stockmann, A.; Kurzawa, J.; Fritz, N.; Acar, N.; Schneider, S.; Daub, J.; Engl, R.; Clark, T. *J. Phys. Chem. A* **2002**, *106*, 7958–7970.

(29) Woo, H. Y.; Liu, B.; Kohler, B.; Korystov, D.; Mikhailovsky, A.; Bazan, G. C. *J. Am. Chem. Soc.* **2005**, *127*, 14721–14729.

(30) (a) Zheng, Q.; He, G. S.; Prasad, P. N. *J. Mater. Chem.* **2005**, *15*, 579–587. (b) Hou, H.; Wei, Y.; Song, Y.; Mi, L.; Tang, M.; Li, L.; Fan, Y. *Angew. Chem., Int. Ed.* **2005**, *44*, 6067–6074.

(31) Corresponding light-field images of the cells to ascertain the locations of the cell nuclei and nucleoli, and costaining experiment to confirm the nucleoli-staining capability of the ligands and complexes, will be carried out in future.